







RESEARCH ARTICLE | FEBRUARY 15 2024

Induced out-of-plane piezoelectricity and giant Rashba spin splitting in Janus $WSiZ_3H$ ($Z = N, P, As$) monolayers toward next-generation electronic devices

Tuan V. Vu ; Bui D. Hoi  ; A. I. Kartamyshev ; Nguyen N. Hieu  

 Check for updates

J. Appl. Phys. 135, 074301 (2024)

<https://doi.org/10.1063/5.0190799>



View
Online



Export
Citation

CrossMark



APL Quantum
Bridging fundamental quantum research with technological applications

Now Open for Submissions
No Article Processing Charges (APCs) through 2024

Submit Today



Induced out-of-plane piezoelectricity and giant Rashba spin splitting in Janus $WSiZ_3H$ ($Z = N, P, As$) monolayers toward next-generation electronic devices

Cite as: J. Appl. Phys. **135**, 074301 (2024); doi: [10.1063/5.0190799](https://doi.org/10.1063/5.0190799)

Submitted: 11 December 2023 · Accepted: 24 January 2024 ·

Published Online: 15 February 2024



View Online



Export Citation



CrossMark

Tuan V. Vu,^{1,2,a)}  Bui D. Hoi,^{3,b)}  A. I. Kartamyshev,^{1,2}  and Nguyen N. Hieu^{4,5,b)} 

AFFILIATIONS

¹Laboratory for Computational Physics, Institute for Computational Science and Artificial Intelligence, Van Lang University, Ho Chi Minh City 70000, Vietnam

²Faculty of Mechanical - Electrical and Computer Engineering, Van Lang University, Ho Chi Minh City 70000, Vietnam

³Department of Physics, University of Education, Hue University, Hue 530000, Vietnam

⁴Institute of Research and Development, Duy Tan University, Da Nang 550000, Vietnam

⁵Faculty of Natural Sciences, Duy Tan University, Da Nang 550000, Vietnam

^{a)}Electronic mail: tuan.vu@vlu.edu.vn

^{b)}Authors to whom correspondence should be addressed: buidinhhoi@hueuni.edu.vn and hieunn@duytan.edu.vn

ABSTRACT

Two-dimensional (2D) piezoelectric nanomaterials have widely been studied recently due to their promise for various applications in technology. Investigation of vertical piezoelectricity will contribute to a deeper understanding of the intrinsic mechanism of piezoelectric effects in the 2D structures. In this paper, we report a first-principle study for the structural, electronic, piezoelectric, and transport properties of new-designed Janus $WSiZ_3H$ ($Z = N, P,$ and As) monolayers. The structural stability of $WSiZ_3H$ is theoretically confirmed based on the energetic, phonon dispersion, and also elastic analyses. At the ground state, while $WSiN_3H$ is an indirect semiconductor, both $WSiP_3H$ and $WSiAs_3H$ are predicted to be direct semiconductors with smaller bandgaps. When the spin-orbit coupling effects are taken into account, a large valley spin splitting is observed at the K point of $WSiZ_3H$ materials. Interestingly, a giant Rashba spin splitting is found in $WSiP_3H$ and $WSiAs_3H$ with Rashba constant α_R up to 770.91 meV Å. Additionally, our first-principles study indicates that Janus $WSiZ_3H$ monolayers are piezoelectric semiconductors with high out-of-plane piezoelectric coefficient $|d_{31}|$, up to 0.15 pm/V, due to the broken mirror symmetry. Besides, with high electron mobilities and also possessing direct band gaps, $WSiP_3H$ and $WSiAs_3H$ monolayers are favorable for applications in optoelectronics.

Published under an exclusive license by AIP Publishing. <https://doi.org/10.1063/5.0190799>

I. INTRODUCTION

Controlling the mechanical and electrical characteristics of nanoscale devices dynamically is one of the biggest obstacles to fully using the power of nanotechnology. The unique aspect of two-dimensional (2D) piezoelectric nanomaterials lies in their ability to convert mechanical strain into electrical energy and vice versa, even at the nanoscale.¹ Piezoelectricity is essential to many different kinds of applications, ranging from sensors and actuators to energy

harvesting devices.^{2,3} The thin and flexible nature of the 2D structures makes them particularly attractive for integration into nanoelectronic devices and wearable technologies.^{4–6} Scientists are presently delving into and manipulating diverse 2D materials to unlock their full potential in the realm of piezoelectricity. The studies of 2D piezoelectric structures not only help us to understand their physical characteristics but also open up new avenues for innovative technologies with enhanced performance and adaptability.⁷

16 February 2024 03:03:44

Recent studies have shown that 2D materials can have many advantages in piezoelectric characteristics.^{8,9} The piezoelectricity has been experimentally reported in a free-standing MoS₂ monolayer.^{10,11} The in-plane piezoelectric coefficient d_{11} of the MoTe₂ material was found to be 9.13 pm/V¹² by the density functional theory (DFT) calculations, much larger than that of the traditional bulk form of α -quartz (2.3 pm/V).¹³ Particularly 2D group IV monochalcogenides exhibit an outstanding piezoelectric effect with d_{11} ranging from 75.43 to 212.13 pm/V.¹⁴ Such positive initial results are worthy of continuing studies on the piezoelectric effect in 2D materials.

Since 2D Janus materials have been reported experimentally,^{15,16} these asymmetric structures have been of particular interest because they possess many rich physical characteristics with many technological application prospects.^{17–20} Many novel characteristics of Janus structures have been found, which do not exist in their corresponding symmetric materials.^{21–24} Recently, Janus XMoSiN₂ ($X = S, Se, Te$) has been designed from the MoSi₂N₄ monolayer.²⁵ The Rashba spin splitting does not often appear in the vertically symmetrical structure. However, the mirror symmetry breaking in Janus materials can give rise to the Rashba spin splitting effects. This is explained by the presence of a perpendicularly internal electric field because of the difference in electronegativity between layers of atoms in the Janus material, such as in the 2D Janus structures based on transition metal dichalcogenide.²⁶ Furthermore, the lack of vertical mirror symmetry may induce the out-of-plane piezoelectric effect in the 2D Janus materials.²⁷ The out-of-plane piezoelectric coefficient d_{31} for Janus γ -Sn₂STe and Sb₂Te₂Se monolayers has theoretically been predicted to be 1.02²⁷ and 1.72 pm/V,²⁸ respectively, which are suitable for piezoelectric devices. In this paper, we theoretically design the novel Janus WSiZ₃H ($Z = N, P, \text{ and } As$) monolayers and systematically examine their structural, electronic, piezoelectric, and transport features based on a first-principles approach.

II. COMPUTATIONAL METHODS

First-principle calculations were carried out with the projector augmented wave (PAW) method^{29,30} as performed in the Vienna *Ab initio* Simulation Package.^{31,32} We used the generalized gradient approximation of Perdew–Burke–Ernzerhof (PBE)³³ to treat the electron exchange–correlation functional. The hybrid functional suggested by Heyd, Scuseria, and Ernzerhof (HSE06)³⁴ was also adopted to get a better examination of the electronic bandgap. The semiempirical DFT–D3 method³⁵ was used to consider the weak van der Waals forces. The spin-orbit coupling (SOC) effect was included in the self-consistent calculations.³⁶ An energy of 650 eV was adopted as the energy cutoff of the plane wave basis set, and the Brillouin zone integration was sampled by a $12 \times 12 \times 1$ k -point mesh grid. The threshold for energy convergence was chosen to be 10^{-6} eV, and the positions of atoms in the studied structures were fully relaxed until the maximum force on each atom was smaller than 10^{-3} eV/Å. A vacuum space of 40 Å was inserted to the vertical direction. Phonon spectra were calculated by the frozen-phonon technique as implemented in the PHONOPY code.³⁷ The *ab initio* molecular dynamics (AIMD) simulation³⁸ with the canonical ensemble was performed at 300 K to examine

the thermal stability. The dipole correction was included to correct the dipole moment induced in the asymmetric structures. The strain–stress relationship and density functional perturbation theory (DFPT) were used to calculate the elastic and piezoelectric coefficients. We adopted the deformation potential (DP) method³⁹ to examine the mobility of the carriers.

III. RESULTS AND DISCUSSION

We show the crystal structures of 2D Janus WSiZ₃H ($Z = N, P, \text{ and } As$) monolayers in Fig. 1(a). At equilibrium, Janus WSiZ₃H belongs to the $P3m1$ (No. 156) space symmetry group. Our calculations indicate that the optimized lattice constants of WSiN₃H, WSiP₃H, and WSiAs₃H are 2.91, 3.42, and 3.57 Å, respectively. These values are very close to those of WSi₂N₄ (2.91 Å), WSi₂N₄ (3.46 Å), and WSi₂N₄ (3.61 Å).⁴⁰ The obtained structural parameters of Janus WSiZ₃H are presented in Table I.

We next evaluate the chemical bonding strength in the studied compound through the calculations for the cohesive energy E_{coh} as follows:

$$E_{\text{coh}} = \frac{E_{\text{tot}} - (N_{\text{W}}E_{\text{W}} + N_{\text{Si}}E_{\text{Si}} + N_{\text{Z}}E_{\text{Z}} + N_{\text{H}}E_{\text{H}})}{N_{\text{W}} + N_{\text{Si}} + N_{\text{Z}} + N_{\text{H}}}, \quad (1)$$

where E_{tot} and E_{η} ($\eta = W, Si, Z, \text{ and } H$) are the total energy of WSiZ₃H and energy of the isolated η element, respectively. N_{η} are the numbers of the η atom in the unit cell.

The electron localization function (ELF) of Janus WSiZ₃H is depicted in Fig. 1(b) to analyze the spatial charge distribution and the unique bonding characteristics in their structures. We can see that the electron in Janus WSiZ₃H monolayers is mainly located around the hydrogen and Z atoms. Meanwhile, the charge density around the W and Si atoms is very low. This suggests that there is an electron transfer from W and Si atoms to H/Z atoms. We show the results of the Bader analysis for Janus WSiZ₃H monolayers in Table I.

The calculated E_{coh} for Janus WSiZ₃H compounds are also listed in Table I. Based on Eq. (1), the material exhibits a stable structure in energy since its cohesive energy is negative. The more energetically stable the structure, the more negative the cohesive energy is. As listed in Table I, the calculated E_{coh} for all three compounds is negative, suggesting that their structure is energetically stable. The most energetically stable structure is indicated to be WSiN₃H with $E_{\text{coh}} = -8.23$ eV/atom. The most energetically stable structure of WSiN₃H is due to their shorter chemical bond lengths in comparison with other compounds. In addition, the Bader charge analysis is also carried out to quantitatively study the distribution and variations in the effective electrons in the studied compounds. As shown in Table I, the hydrogen atoms in WSiP₃H and WSiAs₃H monolayers accumulated additional charge, while a small amount of charge on the hydrogen atom in the WSiN₃H monolayer was lost. This is also clearly shown in the ELF image in Fig. 1(c). The calculated results also indicated that the Si atoms lose charge. However, there are large differences in the amount of charge loss of Si in different monolayers. The atomic charges for Si atoms in WSiN₃H, WSiP₃H, and WSiAs₃H monolayers are $-2.086|e|$, $-0.310|e|$, and $-0.001|e|$, respectively, as reported in Table I.

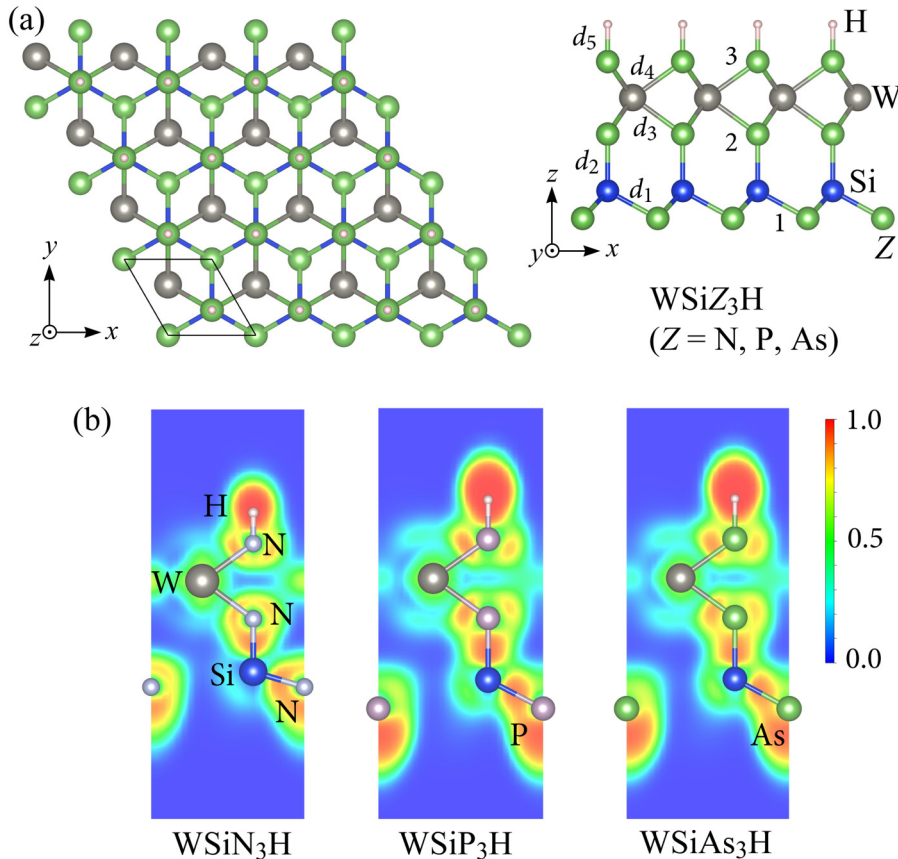


FIG. 1. (a) Crystal structures and (b) calculated contour maps of the electron localization function (ELF) of WSiZ_3H ($Z = \text{N}, \text{P}, \text{As}$) monolayers. The blue and red regions in the ELF maps indicate the lowest (0.0) and highest (1.0) values of ELF, demonstrating the depletion and accumulation of electrons, respectively.

Furthermore, charge polarization in the vertical direction will result from the asymmetry in the vertical charge distributions in each structure. Consequently, Janus WSiZ_3H materials have the out-of-plane piezoelectricity.

To evaluate the structural stability, we carry out the phonon spectra of Janus WSiZ_3H monolayers as depicted in Fig. 2. Since the unit cell of Janus WSiZ_3H contains six atoms, its phonon dispersions have 18 phonon modes. We recognize that, as presented in Fig. 2, there is a vibrational region where both acoustic and optical phonons co-exist. This induces the robust acoustic-optical scattering in the Janus WSiZ_3H . Importantly, there are no negative vibrational frequencies in the phonon dispersion relations of all three investigated structures. This demonstrates that the dynamical stability of Janus WSiZ_3H monolayers is confirmed. Furthermore,

we also evaluate the thermal stability of WSiZ_3H based on the AIMD simulations. The total energy fluctuations to simulation time at 300 K within 10 ps by the AIMD simulation for WSiZ_3H monolayers are depicted in Fig. S1 in the [supplementary material](#). It is found that the crystal structures of WSiZ_3H monolayers remain robust after 10 ps of AIMD simulation. There is no structural transition nor the breaking of chemical bonds. This demonstrates that WSiZ_3H monolayers are thermally stable at room temperature.

We next examine the electronic properties of WSiZ_3H based on the analysis of their electronic band diagrams as shown in Fig. 3. Our calculated results for the band structures indicate that all three configurations of WSiZ_3H are semiconductors. However, while WSiN_3H exhibits indirect semiconducting characteristics

TABLE I. The lattice constant a (Å), bond length d (Å), thickness of monolayer Δh (Å), cohesive energy E_{coh} (eV), and Bader charge q ($|e|$) of atoms for WSiZ_3H monolayers. The sub-indexes $Z(1)$, $Z(2)$, and $Z(3)$ denote the Z atom located in the bottom, middle, and topmost of the monolayer as shown in Fig. 1(a), respectively.

	a	d_1	d_2	d_3	d_4	d_5	Δh	E_{coh}	q_{W}	q_{Si}	$q_{\text{Z}(1)}$	$q_{\text{Z}(2)}$	$q_{\text{Z}(3)}$	q_{H}
WSiN_3H	2.91	1.76	1.74	2.10	2.08	1.02	5.75	-8.23	-1.374	-2.086	1.446	1.347	0.741	-0.075
WSiP_3H	3.42	2.23	2.22	2.44	2.43	1.42	7.53	-6.25	-0.553	-0.310	0.157	0.377	-0.183	0.512
WSiAs_3H	3.57	2.35	2.34	2.55	2.54	1.53	7.99	-5.64	-0.094	-0.001	-0.065	0.071	-0.487	0.576

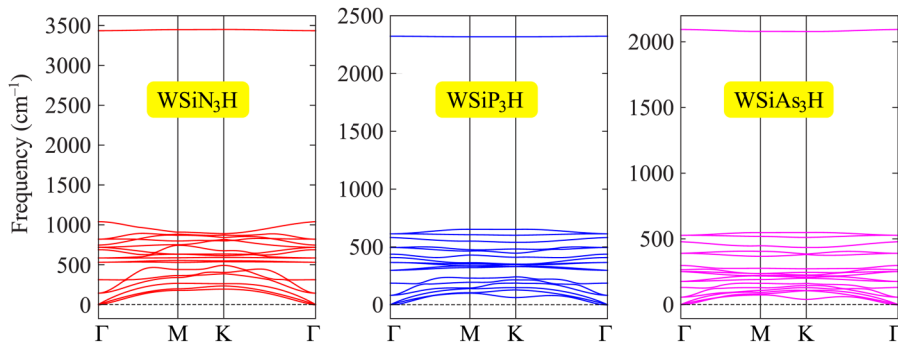


FIG. 2. Phonon dispersions of WSiN₃H, WSiP₃H, and WSiAs₃H monolayers.

with the valence band maximum (VBM) located at the K point and conduction band minimum (CBM) found at the Γ point as revealed in Fig. 3(a), both WSiP₃H and WSiAs₃H monolayers possess the small direct bandgaps opening at the K point. At the PBE level, the bandgaps of WSiN₃H, WSiP₃H, and WSiAs₃H are predicted to be 2.06, 0.65, and 0.58 eV, respectively. Notably, the band structure characteristics of Janus WSiZ₃H are similar to those of WSi₂Z₄ monolayers; for example, WSi₂N₄ exhibits the indirect semiconducting characteristics with energy gap of 2.08 eV,⁴⁰ which is similar to its corresponding Janus WSiZ₃H. To correct the bandgap, we carry out the band structures of Janus WSiZ₃H monolayers calculated by the HSE06 method as illustrated in Fig. 3. The HSE06 calculations give a larger bandgap of the examined materials of 2.63, 0.92, and 0.83 eV for WSiN₃H, WSiP₃H, and WSiAs₃H, respectively, as presented in Table II.

Figure 4 shows the band structures of WSiZ₃H calculated by the PBE+SOC approach. When including the SOC effect, the band structures of Janus WSiZ₃H are significantly changing and the SOC effect slightly reduces the bandgap of the studied materials as listed in Table III. In addition, the spin degeneracy is eliminated when the SOC effect is taken into account. A valley spin splitting λ_Z is found at the K point in the valence band of all three Janus WSiZ₃H materials as shown in Fig. 4. The λ_Z value for WSiN₃H, WSiP₃H, and WSiAs₃H is observed to be 0.42, 0.45, and 0.51 eV, respectively. Furthermore, we also observe the obvious Rashba splitting near the Γ point in the valence band of the Janus WSiP₃H and WSiAs₃H monolayers as shown in Figs. 4(b) and 4(c). We can

describe the strength of the Rashba SOC splitting via three Rashba parameters: Rashba energy E_R , the k -space shift or momentum offset k_R , and Rashba constant α_R . Here, we can get the values of E_R and k_R from the band structures⁴¹ and the Rashba constant α_R is obtained via the expression as $\alpha_R = 2E_R/k_R$ ⁴¹ with the schematic description of the Rashba-type spin splitting at the Γ point illustrated in Fig. 4(d). The calculated Rashba parameters of Janus WSiP₃H and WSiAs₃H monolayers are presented in Table II. It can be seen that there are differences in the Rashba energy in the Γ -K E_R^K and Γ -M E_R^M directions. However, this difference is small. The values of Rashba energy E_R^K for WSiP₃H and WSiAs₃H monolayers are calculated to be 55.9 and 47.3 meV, respectively, which are slightly higher than those in the Γ -M direction. We found the values of E_R^M for WSiP₃H and WSiAs₃H monolayers to be 49.9 and 47.3 meV, respectively. In addition, the momentum offset k_R^K is also quite close to that k_R^K for both two studied systems. From Table II, we can see that the Rashba constants in the Γ -K/ Γ -M directions α_R^K/α_R^M for WSiP₃H and WSiAs₃H monolayers are 621.11/623.75 and 675.71/770.91 meV Å, respectively. The obtained α_R value for WSiZ₃H is comparable with that of Janus MoSeTe (524 meV Å)²⁶ but much higher than that of WSiGeN₄ (111 meV Å).⁴² It is clear that while the dependence of the Rashba parameters of WSiP₃H on the investigated directions in their Brillouin zone is weak, the WSiAs₃H monolayer exhibits slightly anisotropic Rashba spin splitting. The Rashba constants α_R for WSiAs₃H are higher than those for WSiP₃H because the SOC effect in As is larger than that in P.

16 February 2024 03:03:44

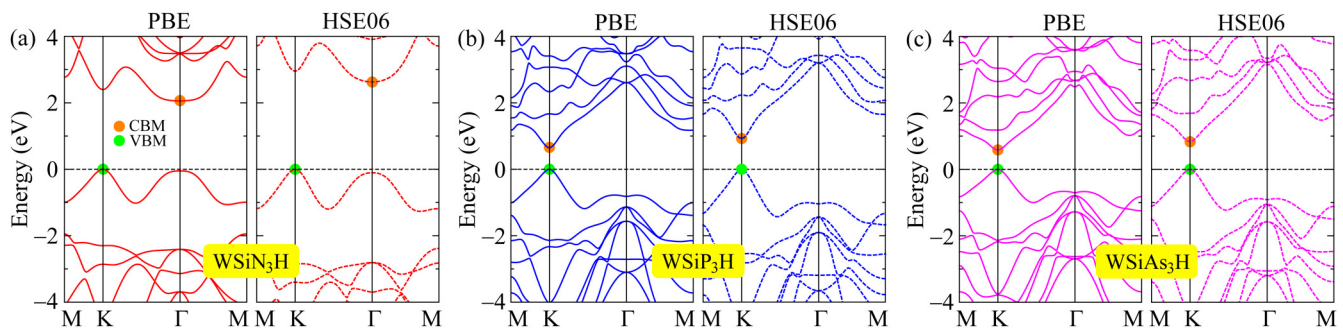


FIG. 3. Calculated PBE (left) and HSE06 (right) band structures of WSiN₃H (a), WSiP₃H (b), and WSiAs₃H (c) monolayers.

TABLE II. The PBE/HSE06/PBE+SOC bandgap E_g (eV), vacuum level difference $\Delta\Phi$ (eV), valley spin splitting energy λ_Z (eV), Rashba energy E_R (meV), momentum offset k_R (\AA^{-1}), Rashba constant α_R (meV \AA), and work function Φ of WSiZ₃H (Z = N, P, As) monolayers. Indexes K and M indicate the Rashba parameters calculated in the Γ -K and Γ -M directions, respectively.

	E_g^{PBE}	E_g^{HSE06}	$E_g^{\text{PBE+SOC}}$	λ_Z	E_R^K	E_R^M	k_R^K	E_R^M	α_R^K	α_R^M	$\Delta\Phi$	Φ_Z	Φ_H
WSiN ₃ H	2.06	2.63	1.85	0.42	2.85	5.06	2.21
WSiP ₃ H	0.65	0.92	0.40	0.45	55.9	49.9	0.18	0.16	621.11	623.75	1.22	4.52	3.30
WSiAs ₃ H	0.58	0.83	0.30	0.51	47.3	42.4	0.14	0.11	675.71	770.91	0.69	4.17	3.48

Another important electronic feature of materials is work function Φ , which can be calculated based on the Fermi level F_I and vacuum level V_I as $\Phi = V_I - F_I$. The values of F_I and V_I can be found by the analysis of the electrostatic potential as shown in Fig. S2 in the [supplementary material](#). Due to the asymmetric structure, WSiZ₃H monolayers possess an intrinsic built-in electric field. Therefore, we include the dipole corrections in the calculations for Janus structures. From Fig. S1 in the [supplementary material](#), we can see that there is a distinct vacuum level difference $\Delta\Phi$ existing on the two different sides of Janus WSiZ₃H monolayers. Consequently, there is a difference in the work function on the two sides Φ_Z and Φ_H as listed in Table II. The calculated results for the work functions show that the value of Φ_Z is always higher than that of Φ_H for all three materials, demonstrating that the electrons escape more easily from the H side than the Z side. Differences in the electrostatic potential at the surfaces of WSiZ₃H not only affect the work function but also affect their other chemical properties, including photocatalytic characteristics.⁴³

Piezoelectric materials are strongly restricted by their crystal symmetry, and the necessary condition for piezoelectric material is the lack of central symmetry. Since WSiZ₃H materials are semiconductors with non-centrosymmetric structure, we can consider them as piezoelectric materials. The piezoelectric properties are the ground state features; therefore, the DFT approach is a suitable technique for the piezoelectricity examination.¹⁴ Importantly, the correctness of earlier DFT computed findings for the piezoelectricity of MoS₂ by Duerloo *et al.*¹² has been validated by recent

experimental measurement.¹⁰ Then, we utilize the identical methodology as Duerloo *et al.*¹² in order to investigate the piezoelectric characteristics of Janus WSiZ₃H monolayers.

To examine the piezoelectricity, we first calculate the planar elastic stiffness coefficients C_{ij} by fitting the strain-dependent unit-cell energy.¹² In the strained unit cell, the positions of atoms are allowed to be fully relaxed and the obtained corresponding coefficients in this model are so-called relaxed-ion stiffness coefficients. The relaxed-ion stiffness coefficients, which represent the piezoelectricity from contribution of both electronic and ionic components, are considered to be in better agreement with experimental measurements than the clamped-ion model.^{14,44} For the strain energy calculations, small uniaxial strains from -1.5% to 1.5% (in increments of 0.5%) are applied. For Janus WSiZ₃H monolayers, only two independent coefficients C_{11} and C_{12} should be carried out [$C_{22} = C_{11}$ and $C_{66} = (C_{11} - C_{12})/2$]. The calculated relaxed-ion C_{ij} and also corresponding Young's modulus $Y_{2D} = (C_{11}^2 - C_{12}^2)/C_{11}$ and Poisson's ratio $\nu = C_{12}/C_{11}$ are listed in Table III. Due to hexagonal symmetry, Janus WSiZ₃H monolayers are mechanically isotropic. We can see that the in-plane elastic coefficients of WSiZ₃H materials are positive and they satisfy Born's mechanical stability criteria for 2D hexagonal crystal,⁴⁵ namely, $C_{11} > 0$ and $C_{66} > 0$. This demonstrates that the mechanical stability of Janus WSiZ₃H monolayers is confirmed. Furthermore, WSiZ₃H monolayers, particular Janus WSiN₃H, exhibit high Young's modulus Y_{2D} . The value of Y_{2D} for WSiN₃H, WSiP₃H, and WSiAs₃H is calculated to be 373.83, 153.47, and 124.80 N/m,

16 February 2024 03:03:44

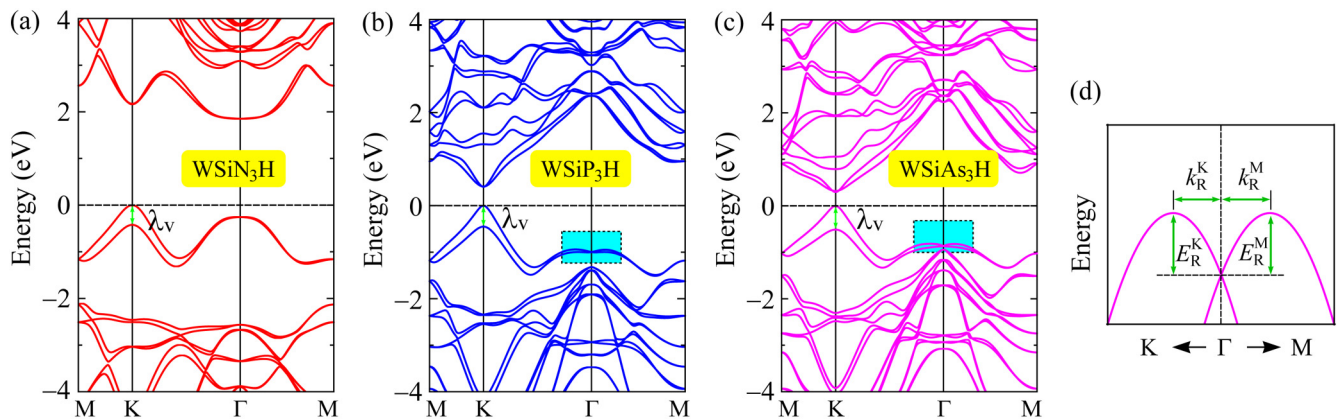


FIG. 4. Calculated PBE+SOC band structures of WSiN₃H (a), WSiP₃H (b), and WSiAs₃H (c) monolayers. (d) The schematic diagram of Rashba spin splitting that corresponds to the shadow regions around the Γ point in the valence band in (b) and (c).

TABLE III. The relaxed-ion elastic coefficient C_{ij} (N/m), Young modulus Y_{2D} (N/m), Poisson ratio ν , and piezoelectric coefficients e_{11} (10^{-10} C/m), e_{31} (10^{-10} C/m), d_{11} (pm/V), and d_{31} (pm/V) of WSiZ₃H monolayers.

	C_{11}	C_{12}	C_{66}	Y_{2D}	ν	e_{11}	e_{31}	d_{11}	d_{31}
WSiN ₃ H	402.86	108.15	147.35	373.83	0.27	2.90	-0.08	0.99	-0.02
WSiP ₃ H	162.88	41.17	60.85	152.47	0.25	5.92	-0.16	4.86	-0.08
WSiAs ₃ H	136.13	39.27	48.43	124.80	0.29	6.36	-0.26	6.57	-0.15

respectively. The Young modulus of WSiN₃H is comparable with that of graphene (340 N/m)⁴⁶ and much higher than that of MoS₂ (130 N/m)⁴⁷ and Janus MoSSe (113 N/m).⁴⁸ This suggests that the Janus WSiN₃H monolayer is a very mechanically hard material.

The polarization of the noncentrosymmetric systems can be changed by uniaxial strain. We examine the linear piezoelectric coefficients based on evaluating the polarization change under the applied uniaxial strains within the framework of the modern theory of polarization.⁴⁹ The linear piezoelectric effect in 2D structures can be described through the third-rank piezoelectric tensors e_{ijk} and d_{ijk} , which depend on the relationship between the surface polarization \bar{P}_i and strain ϵ_{jk} or stress σ_{jk} as¹²

$$e_{ijk} = \frac{\partial P_i}{\partial \epsilon_{jk}}, \quad (2)$$

$$d_{ijk} = \frac{\partial P_i}{\partial \sigma_{jk}}, \quad (3)$$

where indices $i, j, k \in \{1, 2, 3\}$ with 1, 2, and 3 correspond to x, y , and z , respectively.

In the case of Janus WSiZ₃H monolayers, due to the break of the vertical symmetry, both in-plane e_{11} and out-of-plane e_{31} piezoelectric coefficients are available when the uniaxial strain is introduced. The piezoelectric coefficients can be obtained by using the density functional perturbation theory (DFPT) and we then derive the coefficients d_{ij} using the relations with the previously obtained e_{jk} and elastic coefficients C_{ij} as⁵⁰

$$d_{11} = \frac{e_{11}}{C_{11} - C_{12}}, \quad (4)$$

$$d_{31} = \frac{e_{31}}{C_{11} + C_{12}}. \quad (5)$$

We apply the uniaxial strains along the x and y directions of the orthorhombic supercell to calculate the coefficients e_{11} and e_{31} . The obtained e_{11} and e_{31} and corresponding d_{11} and d_{31} for Janus WSiZ₃H are listed in Table III. We can see that e_{11} for WSiN₃H, WSiP₃H, and WSiAs₃H is 2.90×10^{-10} , 5.92×10^{-10} , and 6.36×10^{-10} C/m, respectively. The obtained e_{11} for Janus WSiZ₃H monolayers is comparable to that of Janus MoS₂ (3.70×10^{-10}),⁵¹ Janus MoSTe (4.55×10^{-10})⁵² or Janus γ -Sn₂STe (4.26×10^{-10}).²⁷ Our calculations indicate that the Janus WSiN₃H monolayer has the smallest piezoelectric response with $d_{11} = 0.99$ pm/V and $d_{31} = -0.02$ pm/V, as presented in Table III. Interestingly, the piezoelectric effect is enhanced by the moving upward of the Z

element from N to As. The magnitude of piezoelectric coefficients for WSiAs₃H is the highest, being $d_{11} = 6.57$ pm/V and $d_{31} = -0.15$ pm/V. This tendency to vary the piezoelectric effect with atomic size has also been found in transition metal dichalcogenides¹² or group IV monochalcogenides.¹⁴ We can see that the in-plane piezoelectric coefficient d_{11} for WSiN₃H (0.99 pm/V) and WSiP₃H (4.86 pm/V) is higher than that of their corresponding symmetric structures WSi₂N₄ (0.25 pm/V) and WSi₂P₄ (1.65 pm/V).⁵³ It is worth noting that the out-of-plane piezoelectricity induced in Janus WSiZ₃H monolayers due to the breaking of mirror symmetry is significant, and the value of d_{31} ranges from -0.02 to -0.15 pm/V. This amplitude of d_{31} is comparable to that of other 2D hexagonal structures, including GaAs (0.125 pm/V),⁵⁴ Janus MoSiGeN₄ (-0.014 pm/V),⁴² or Janus group III monochalcogenides (0.07–0.46 pm/V).⁵⁰ However, the out-of-plane piezoelectric effect in Janus WSiZ₃H monolayers is significantly weaker than that in Janus MoSTe ($d_{31} = 0.40$ pm/V) or Janus γ -Sn₂STe ($d_{31} = 1.02$ pm/V).²⁷

In the last part, we investigate the transport characteristics of WSiZ₃H monolayers. The carrier mobility of semiconductors can be examined by using Bardeen–Shockley deformation potential (DP) theory.³⁹ The mobility of carrier for the 2D structures μ_{2D} is given by⁴²

$$\mu_{2D} = \frac{e\hbar^3 C_{2D}}{k_B T m^* \bar{m}^* E_d^2}, \quad (6)$$

where T is the temperature; m^* is the effective mass; and $\bar{m}^* = \sqrt{m_x^* m_y^*}$ indicates the average effective mass. C_{2D} and E_d are the 2D elastic modulus and DP constant, respectively. In the calculations for the carrier mobility, we adopt $T = 300$ K.

In Table IV, we show the calculated results for the carrier effective masses along the x and y axes m_x^* and m_y^* . It is demonstrated that, except for the WSiN₃H monolayer, the effective masses of both the electron and hole in WSiP₃H and WSiAs₃H monolayers are quite small. This is consistent with their energy band structures displayed in Fig. 3. The difference in the mass between electrons and holes in WSiP₃H and WSiAs₃H monolayers is small. However, the effective masses of both electron and hole exhibit slightly directional anisotropic along the x and y axes as revealed in Table IV. The transport parameters C_{2D} and E_d , which can be obtained by fitting the uniaxial-strain-dependent total energy and band edges as shown in Fig. S3 in the supplementary material, and the corresponding carrier mobilities μ are displayed in Table IV in the supplementary material. It is indicated that the WSiN₃H monolayer possesses very low-electron mobility, about

TABLE IV. Calculated effective mass m^* (in units of free electron mass m_0), 2D elastic modulus C_{2D} (N m^{-1}), DP constant E_d (eV), and carrier mobility μ ($\text{cm}^2 \text{V}^{-1} \text{s}^{-1}$) along the x and y directions of Janus WSiZ_3H .

		m_x^*	m_y^*	C_{2D}^x	C_{2D}^y	E_d^x	E_d^y	μ_x	μ_y
Electron	WSiN_3H	8.09	6.42	228.99	228.95	-3.10	-3.10	8.70	10.96
	WSiP_3H	0.37	0.24	107.42	107.37	-7.17	-7.17	403.21	610.61
	WSiAs_3H	0.53	0.34	90.04	90.03	-6.34	-6.34	209.91	327.11
Hole	WSiN_3H	0.60	0.49	228.99	228.95	-5.93	-5.94	426.42	526.86
	WSiP_3H	0.41	0.26	107.42	107.37	-5.45	-5.45	562.78	882.08
	WSiAs_3H	0.46	0.31	90.04	90.03	-4.77	-4.77	490.74	728.07

only $10 \text{ cm}^2 \text{V}^{-1} \text{s}^{-1}$, due to its large effective mass. The carrier mobility in all three structures exhibits slightly directional anisotropies along the two examined directions. The Janus WSiP_3H monolayer has the highest electron mobility, up to $610.61 \text{ cm}^2 \text{V}^{-1} \text{s}^{-1}$ along the y axis. The electron mobilities μ_x and μ_y of the WSiAs_3H monolayer are found to be 209.91 and $327.11 \text{ cm}^2 \text{V}^{-1} \text{s}^{-1}$, respectively. In addition, the hole mobilities of WSiZ_3H monolayers are high, ranging from 426.42 (μ_x of WSiN_3H) to $882.08 \text{ cm}^2 \text{V}^{-1} \text{s}^{-1}$ (μ_y of WSiP_3H).

IV. CONCLUSION

In conclusions, we have examined the electronic, piezoelectric, and transport properties of novel Janus WSiZ_3H monolayers. We have identified the structural stability of novel Janus WSiZ_3H materials. Our first-principles simulations reveal that WSiZ_3H are semiconductors with large valley spin splitting energy when the SOC is included. Particularly, WSiP_3H and WSiAs_3H monolayers possess the intrinsic Rashba-type spin splitting due to the broken mirror symmetry. The Janus WSiZ_3H monolayers are predicted to be piezoelectric materials with large in-plane piezoelectric coefficients d_{11} up to 6.57 pm/V . Moreover, the breaking of mirror symmetry in Janus structures induces an out-of-plane piezoelectricity with d_{31} from 0.02 to 0.15 pm/V (absolute value). Our calculations also indicate that both WSiP_3H and WSiAs_3H monolayers are the direct bandgap semiconductors with very high electron mobility, indicating that they are more favorable than WSiN_3H for applications in optoelectronic devices.

SUPPLEMENTARY MATERIAL

See the supplementary material for the calculated results for the AIMD simulations, average plane electrostatic potentials, and uniaxial strain-dependence of the total energy and band edge positions of Janus WSiZ_3H ($Z = \text{N, P, As}$) monolayers.

AUTHOR DECLARATIONS

Conflict of Interest

The authors have no conflicts to disclose.

Author Contributions

Tuan V. Vu: Conceptualization (equal); Formal analysis (equal); Investigation (equal); Methodology (equal); Validation (equal). **Bui D. Hoi:** Conceptualization (equal); Formal analysis (equal); Investigation (equal); Validation (equal). **A. I. Kartamyshev:**

Conceptualization (equal); Investigation (equal); Software (equal); Validation (equal). **Nguyen N. Hieu:** Conceptualization (equal); Formal analysis (equal); Investigation (equal); Methodology (equal); Supervision (equal); Validation (equal); Writing – original draft (equal); Writing – review & editing (equal).

DATA AVAILABILITY

The data that support the findings of this study are available from the corresponding authors upon reasonable request.

REFERENCES

- Z. L. Wang, *Adv. Mater.* **24**, 4632 (2012).
- X. Wang, J. Zhou, J. Song, J. Liu, N. Xu, and Z. L. Wang, *Nano Lett.* **6**, 2768 (2006).
- M. Lanza, M. Reguant, G. Zou, P. Lv, H. Li, R. Chin, H. Liang, D. Yu, Y. Zhang, Z. Liu, and H. Duan, *Adv. Mater. Interfaces* **1**, 1300101 (2014).
- N. T. Hiep, C. Q. Nguyen, and N. N. Hieu, *Appl. Phys. Lett.* **123**, 092102 (2023).
- T. C. Phong and L. T. T. Phuong, *Physica B* **666**, 415119 (2023).
- T. C. Phong, V. T. T. Vi, and L. T. T. Phuong, *Phys. Lett. A* **480**, 128946 (2023).
- M. T. Ong and E. J. Reed, *ACS Nano* **6**, 1387 (2012).
- W. Ma, J. Lu, B. Wan, D. Peng, Q. Xu, G. Hu, Y. Peng, C. Pan, and Z. L. Wang, *Adv. Mater.* **32**, 1905795 (2020).
- B. Akçenc, H. E. Ersan, T. Altalhi, M. Yagmurcukardes, and B. Yakobson, *Solid State Commun.* **368**, 115175 (2023).
- H. Zhu, Y. Wang, J. Xiao, M. Liu, S. Xiong, Z. J. Wong, Z. Ye, Y. Ye, X. Yin, and X. Zhang, *Nat. Nanotechnol.* **10**, 151 (2014).
- W. Wu, L. Wang, Y. Li, F. Zhang, L. Lin, S. Niu, D. Chenet, X. Zhang, Y. Hao, T. F. Heinz, J. Hone, and Z. L. Wang, *Nature* **514**, 470 (2014).
- K.-A. N. Duerloo, M. T. Ong, and E. J. Reed, *J. Phys. Chem. Lett.* **3**, 2871 (2012).
- R. Bechmann, *Phys. Rev.* **110**, 1060 (1958).
- R. Fei, W. Li, J. Li, and L. Yang, *Appl. Phys. Lett.* **107**, 173104 (2015).
- A.-Y. Lu, H. Zhu, J. Xiao, C.-P. Chuu, Y. Han, M.-H. Chiu, C.-C. Cheng, C.-W. Yang, K.-H. Wei, Y. Yang, Y. Wang, D. Sokaras, D. Nordlund, P. Yang, D. A. Muller, M.-Y. Chou, X. Zhang, and L.-J. Li, *Nat. Nanotechnol.* **12**, 744 (2017).
- J. Zhang, S. Jia, I. Kholmanov, L. Dong, D. Er, W. Chen, H. Guo, Z. Jin, Y. B. Shenoy, L. Shi, and J. Lou, *ACS Nano* **11**, 8192 (2017).
- M. Yagmurcukardes, Y. Qin, S. Ozen, M. Sayyad, F. M. Peeters, S. Tongay, and H. Sahin, *Appl. Phys. Rev.* **7**, 011311 (2020).
- B. Akçenc, E. Vatanserver, and F. Ersan, *Phys. Rev. Mater.* **5**, 083403 (2021).
- D. H. Ozbey, M. E. Kilic, and E. Durgun, *Phys. Rev. Appl.* **17**, 034043 (2022).
- B. Akçenc, *Comput. Mater. Sci.* **171**, 109231 (2020).
- Y. Z. Abdullahi, A. Bakhtatou, Y. Mogulkoc, and F. Ersan, *J. Phys. Chem. Solids* **175**, 111203 (2023).

- ²²M. Yagmurcukardes, Y. Mogulkoc, B. Akgenc, A. Mogulkoc, and F. M. Peeters, *Phys. Rev. B* **104**, 045425 (2021).
- ²³T. V. Vu, V. T. T. Vi, H. V. Phuc, A. I. Kartamyshev, and N. N. Hieu, *Phys. Rev. B* **104**, 115410 (2021).
- ²⁴N. N. Hieu, H. V. Phuc, A. I. Kartamyshev, and T. V. Vu, *Phys. Rev. B* **105**, 075402 (2022).
- ²⁵R. Sibatov, R. Meftakhtudinov, and A. Kochaev, *Appl. Surf. Sci.* **585**, 152465 (2022).
- ²⁶T. Hu, F. Jia, G. Zhao, J. Wu, A. Stroppa, and W. Ren, *Phys. Rev. B* **97**, 235404 (2018).
- ²⁷T. V. Vu, H. V. Phuc, A. I. Kartamyshev, and N. N. Hieu, *Appl. Phys. Lett.* **122**, 061601 (2023).
- ²⁸J. Qiu, H. Li, X. Chen, B. Zhu, H. Guo, F. Zhang, Z. Ding, L. Lang, J. Yu, and J. Bao, *J. Appl. Phys.* **129**, 125109 (2021).
- ²⁹P. E. Blöchl, *Phys. Rev. B* **50**, 17953 (1994).
- ³⁰G. Kresse and D. Joubert, *Phys. Rev. B* **59**, 1758 (1999).
- ³¹G. Kresse and J. Furthmüller, *Phys. Rev. B* **54**, 11169 (1996).
- ³²G. Kresse and J. Furthmüller, *Comput. Mater. Sci.* **6**, 15 (1996).
- ³³J. P. Perdew, K. Burke, and M. Ernzerhof, *Phys. Rev. Lett.* **77**, 3865 (1996).
- ³⁴J. Heyd, G. E. Scuseria, and M. Ernzerhof, *J. Chem. Phys.* **118**, 8207 (2003).
- ³⁵S. Grimme, J. Antony, S. Ehrlich, and H. Krieg, *J. Chem. Phys.* **132**, 154104 (2010).
- ³⁶A. H. MacDonald, W. E. Pickett, and D. D. Koelling, *J. Phys. C: Solid State Phys.* **13**, 2675 (1980).
- ³⁷A. Togo, L. Chaput, and I. Tanaka, *Phys. Rev. B* **91**, 094306 (2015).
- ³⁸S. Nosé, *J. Chem. Phys.* **81**, 511 (1984).
- ³⁹J. Bardeen and W. Shockley, *Phys. Rev.* **80**, 72 (1950).
- ⁴⁰L. Wang, Y. Shi, M. Liu, A. Zhang, Y.-L. Hong, R. Li, Q. Gao, M. Chen, W. Ren, H.-M. Cheng, Y. Li, and X.-Q. Chen, *Nat. Commun.* **12**, 2361 (2021).
- ⁴¹S. Singh and A. H. Romero, *Phys. Rev. B* **95**, 165444 (2017).
- ⁴²S.-D. Guo, W.-Q. Mu, Y.-T. Zhu, R.-Y. Han, and W.-C. Ren, *J. Mater. Chem. C* **9**, 2464 (2021).
- ⁴³A. Huang, W. Shi, and Z. Wang, *J. Phys. Chem. C* **123**, 11388 (2019).
- ⁴⁴K. H. Michel, D. Çakır, C. Sevik, and F. M. Peeters, *Phys. Rev. B* **95**, 125415 (2017).
- ⁴⁵R. C. Andrew, R. E. Mapasha, A. M. Ukpong, and N. Chetty, *Phys. Rev. B* **85**, 125428 (2012).
- ⁴⁶C. Lee, X. Wei, J. W. Kysar, and J. Hone, *Science* **321**, 385 (2008).
- ⁴⁷R. C. Cooper, C. Lee, C. A. Marianetti, X. Wei, J. Hone, and J. W. Kysar, *Phys. Rev. B* **87**, 035423 (2013).
- ⁴⁸S.-D. Guo, *Phys. Chem. Chem. Phys.* **20**, 7236 (2018).
- ⁴⁹R. D. King-Smith and D. Vanderbilt, *Phys. Rev. B* **47**, 1651 (1993).
- ⁵⁰Y. Guo, S. Zhou, Y. Bai, and J. Zhao, *Appl. Phys. Lett.* **110**, 163102 (2017).
- ⁵¹M. Yagmurcukardes, C. Sevik, and F. M. Peeters, *Phys. Rev. B* **100**, 045415 (2019).
- ⁵²L. Dong, J. Lou, and V. B. Shenoy, *ACS Nano* **11**, 8242 (2017).
- ⁵³S.-D. Guo, Y.-T. Zhu, W.-Q. Mu, L. Wang, and X.-Q. Chen, *Comput. Mater. Sci.* **188**, 110223 (2021).
- ⁵⁴M. N. Blonsky, H. L. Zhuang, A. K. Singh, and R. G. Hennig, *ACS Nano* **9**, 9885 (2015).